

Tracking surface ozone responses to clean air actions under a warming climate in China using machine learning

Jie Fang¹, Yunjiang Zhang^{1*}, Didier Hauglustaine², Bo Zheng³, Ming Wang¹, Jingyi Li¹, Yong Sun⁴, Haiwei Li¹, Junfeng Wang¹, Yun Wu¹, Bin Yuan⁵, Mindong Chen¹,
Xinlei Ge⁶

¹Jiangsu Key Laboratory of Atmospheric Environment Monitoring and Pollution Control, School of Environmental Science and Engineering, Nanjing University of Information Science and Technology, Nanjing 210044, China

²Laboratoire des Sciences du Climat et de l'Environnement, CNRS-CEA-UVSQ, Université Paris-Saclay, Gif-sur-Yvette, France

³Institute of Environment and Ecology, Tsinghua Shenzhen International Graduate School, Tsinghua University, Shenzhen 518055, China

⁴State Key Laboratory of Tibetan Plateau Earth System, Environment and Resources, Institute of Tibetan Plateau Research, Chinese Academy of Sciences, Beijing 100101, China

⁵College of Environment and Climate, Institute for Environmental and Climate Research, Guangdong-Hongkong-Macau Joint Laboratory of Collaborative Innovation for Environmental Quality, Jinan University, Guangzhou 511443, China

⁶School of Energy and Environment, Southeast University, Nanjing 210096, China

Correspondence to: Yunjiang Zhang (yjzhang@nuist.edu.cn)

21 **Abstract.** Surface ozone, a major air pollutant with important implications for human health,
22 ecosystems, and climate, shows long-term trends shaped by both anthropogenic and climatic drivers.
23 Here, we developed a machine learning-based approach, namely the fixed emission approximation
24 (FEA), to disentangle the effects of meteorological variability and anthropogenic emissions on
25 summertime ozone trends in China under the clean air actions. Anthropogenic emissions drove an
26 approximately $+23.2 \pm 1.1 \mu\text{g m}^{-3}$ increase in summer maximum daily 8-hour average ozone during
27 2013–2017, followed by an approximately $-4.6 \pm 1.5 \mu\text{g m}^{-3}$ decrease between 2017 and 2020 in
28 response to strengthened emission controls. In contrast, meteorological anomalies, including
29 heatwaves and rainfall conditions, emerged as key drivers of ozone variability during 2020–2023.
30 Satellite-derived formaldehyde-to-nitrogen dioxide ratios revealed widespread urban volatile
31 organic compounds-limited regimes for ozone production, with a shift toward nitrogen oxides-
32 limited sensitivity under influence of heatwaves. Extending the FEA framework to assess long-term
33 climate influences from 1970 to 2023, we find that sustained climate warming has driven a
34 substantial increase in urban summertime ozone in China. These results demonstrate that climate
35 change was increasingly offsetting the benefits of emission reductions and highlight the need for
36 integrated ozone mitigation strategies that jointly address emission controls and climate adaptation
37 in a warming world.

38 **1 Introduction**

39 Surface ozone (O_3) is a critical air pollutant that poses significant threats to human health (Knowlton et
40 al., 2004), ecosystems (Agathokleous et al., 2020), and climate (Fishman et al., 1979; Hauglustaine et
41 al., 1994). It forms through complex photochemical reactions involving nitrogen oxides (NO_x) and
42 volatile organic compounds (VOCs) in the presence of sunlight (Jacob, 2000; Wang et al., 2017),
43 exhibiting a nonlinear response to its precursors (Guo et al., 2023; Liu and Shi, 2021; Wang et al., 2023a).
44 Controlling ozone pollution remains a global environmental challenge. In recent years, China has
45 implemented a series of national clean air actions, most notably the Air Pollution Prevention and Control
46 Action Plan (2013–2017) and the Three-Year Action Plan for Winning the Blue-Sky War (2018–2020)
47 (Geng et al., 2024; Zhang et al., 2019; Zheng et al., 2018), that have markedly improved air quality,
48 particularly by reducing fine particulate matter ($PM_{2.5}$) (Geng et al., 2024; Zhang et al., 2019). However,
49 surface ozone levels have continued to rise in many regions, raising concerns over the complex drivers
50 of ozone trends and highlighting the need for scientific attribution to guide effective mitigation strategies
51 (Li et al., 2019a; Liu et al., 2023; Wang et al., 2023a; Weng et al., 2022).

52 Long-term ozone variability is jointly influenced by anthropogenic emissions and weather
53 conditions as well as regional climate (Hallquist et al., 2016; Li et al., 2019b; Wang et al., 2022a). While
54 emission controls directly regulate precursor abundance, climate change modulates ozone through
55 chemical feedbacks, meteorological dynamics, and biosphere–atmosphere interactions (Ma and Yin,
56 2021; Xue et al., 2020). Over the past century, global surface temperatures have substantially increased
57 relative to the pre-industrial baseline (1850–1900), driven largely by human activities (IPCC, 2021). In
58 such a warming world, extreme climate anomalies – such as heatwaves and persistent rainfall shifts –
59 were expected to be intensified (Li et al., 2025a; Li et al., 2025b). These events were increasingly
60 recognized as critical modulators of ozone variability through their impacts on photochemistry and
61 precursor emissions (Gao et al., 2023; Pu et al., 2017; Wang et al., 2022a).

62 Quantifying the respective roles of anthropogenic emissions and meteorological variability in
63 driving ozone trends is therefore essential for evaluating the effectiveness of clean air policies (Li et al.,
64 2019a; Liu et al., 2023). Previous studies have reported rapid increases in surface ozone concentrations

65 in urban cluster regions in China – such as the Beijing–Tianjin–Hebei (BTH) and Yangtze River Delta
66 (YRD) – during the **Phase I** (2013 – 2017), with increases of approximately 28% and 18%, respectively
67 (Chen et al., 2020; Li et al., 2019a; Liu et al., 2023). In contrast, a modest decline in ozone levels was
68 observed during 2018 – 2020, largely attributed to emission reductions (Li et al., 2021; Liu and Wang,
69 2020b; Wang et al., 2024b; Wang et al., 2023a). However, since 2021, observations indicate a renewed
70 increase in ozone concentrations (Fig. S1). These fluctuations suggest oscillating trends over the past
71 decade, the drivers of which remain poorly constrained.

72 Two main approaches have been applied to attribute air pollution trends: chemical transport models
73 (CTMs) (Li et al., 2021; Liu et al., 2023; Liu and Wang, 2020a) and data-driven statistical frameworks
74 (Li et al., 2019a; Li et al., 2019b; Li et al., 2020). The CTMs simulate atmospheric composition based
75 on emission inventories, meteorological fields, and chemical mechanisms (Ivatt et al., 2022; Liu and Shi,
76 2021; Liu et al., 2023; Ye et al., 2024). They allow attribution of trend components to emissions or
77 meteorology, and can also resolve sector-specific impacts. However, these models face challenges,
78 including uncertainties and temporal lags in emission inventories. Statistical models, on the other hand,
79 rely on observational datasets and predictor-response relationships without requiring explicit emissions
80 or chemical schemes (Li et al., 2019a; Li et al., 2019b; Li et al., 2020; Zhai et al., 2019). With the growing
81 availability of atmospheric big data, machine learning models have emerged as useful tools for trend
82 attribution (Dai et al., 2023; Grange et al., 2018; Vu et al., 2019; Zhang et al., 2025; Zheng et al., 2023).
83 For instance, Grange et al. (2018) developed a random forest-based framework to isolate meteorological
84 influences on particulate matter. Similarly, Wang et al. (2023) used an enhanced extreme gradient
85 boosting (XGBoost) model to analyze spatial and temporal ozone patterns in China from 2010 to 2021,
86 confirming that emission reductions played a key role in recent declines. Other recent efforts have
87 extended statistical models to long-term assessments of air pollution drivers under climate change (Wang
88 et al., 2022b).

89 Here, we developed a **machine learning-based model framework** – fixed emission approximation
90 (FEA) – to quantify the **relative contribution** of anthropogenic emissions and meteorological conditions
91 in shaping summertime surface ozone trends in China. Applying the FEA to nationwide observational
92 data from 2013 to 2023, we identified three phases of ozone evolution corresponding to the major clean
93 air actions. We further analyzed short-term ozone anomalies associated with extreme weather events,

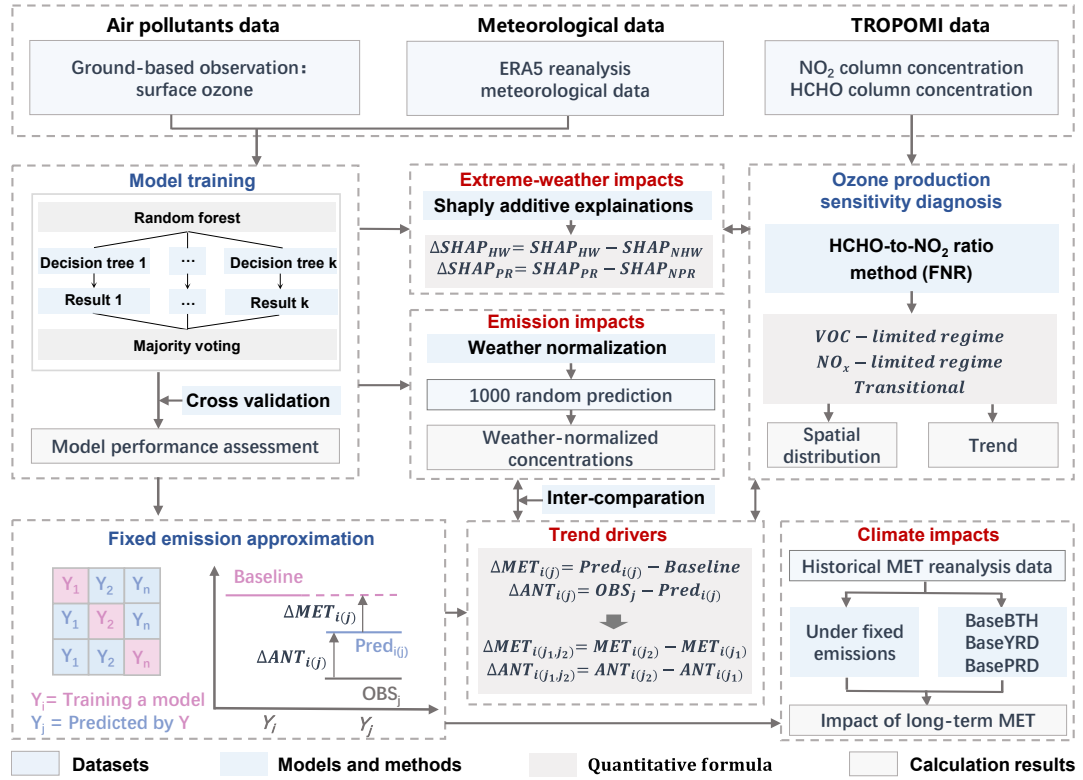
94 such as the 2022 heatwave and seasonal rainfall. To characterize ozone production regimes, we integrated
95 satellite-derived formaldehyde-to-nitrogen dioxide (HCHO/NO₂, FNR) ratios from the tropospheric
96 monitoring instrument (TROPOMI), revealing spatiotemporal shifts in ozone formation sensitivity
97 across China. Finally, we extend our FEA analysis to evaluate climate-driven ozone trends from 1970 to
98 2023, using historical meteorological reanalysis data. Collectively, these analyses provide an integrated
99 understanding of how anthropogenic and climatic factors jointly shape surface ozone dynamics under a
100 warming climate.

101 **2 Data and methods**

102 **2.1 Data sources and methodology overview**

103 Figure 1 provides an overview of the data analysis and methodological framework employed in this
104 study. We first integrated multi-dimensional datasets, including hourly surface air pollutant
105 concentrations, meteorological reanalysis fields, and satellite remote sensing data. Hourly surface
106 observations of ozone, nitrogen dioxide (NO₂), carbon monoxide (CO), and fine particulate matter (PM_{2.5})
107 were accessed from the National Environmental Monitoring Center of China through the open website
108 <https://air.cnemc.cn:18007/> (last accessed: May 20, 2024). Hourly meteorological data with a spatial
109 resolution of 0.25° × 0.25° were sourced from the ERA5 reanalysis dataset provided by the European
110 Centre for Medium-Range Weather Forecasts (ECMWF) and are available for download at
111 <https://cds.climate.copernicus.eu> (last accessed: March 20, 2025). Detailed variables are listed in Table
112 S1. The time variables – hour (hour of day) and month (month of year) – are used as emission surrogates
113 to capture regular diurnal and seasonal variations in anthropogenic activity. A similar strategy is widely
114 applied in previous studies about long-term trends in air pollutants (e.g., Grange et al., 2018; Vu et al.,
115 2019) to separate short-term cyclical emission variability from long-term trends. For 2013 – 2014, the
116 surface MDA8 ozone data were obtained from the Tracking Air Pollution in China (TAP) dataset (Geng
117 et al., 2021), which can be downloaded from <http://tapdata.org> (last accessed: May 20, 2024). The
118 TROPOMI on the Sentinel-5P satellite provides global continuous observation data for two indicators of
119 ozone precursors: NO₂ and formaldehyde (HCHO) column concentrations (Lamsal et al., 2014; Shen et
120 al., 2019). The FNR was used as a proxy for VOC/NO_x reactivity and as a diagnostic indicator of ozone

121 formation sensitivity (Sillman, 1995), to explain and verify the impact of extreme weather and
 122 anthropogenic emissions on ozone. Details of the ozone sensitivity diagnostic method are provided in
 123 Text S1.



140 levels. These temporal emission surrogates, including month and hour, represent short-term regular
141 emission patterns (e.g., diurnal cycles), thereby enabling the model to isolate the long-term emission-
142 driven component of ozone changes (Grange et al., 2018; Meng et al., 2025; Shi et al., 2021; Vu et al.,
143 2019). The meteorological parameters include 18 distinct variables at different altitudes (see Table S1).
144 It should be noteworthy that surface air pollutant observations for each city represent multi-site averages
145 rather than data from a single monitoring station, which reduces the influence of local representativeness
146 **uncertainty**. The meteorological data are obtained from the nearest grid cell corresponding to each city,
147 ensuring spatial consistency between the pollutant and meteorological datasets. This approach was
148 similar to the methodologies widely adopted in previous studies (Shi et al., 2021; Wang et al., 2025; Yao
149 et al., 2024; Zheng et al., 2023). Our modeling strategy involves building and predicting models for
150 individual cities and for each year from 2015 to 2023, which helps in minimizing the uncertainty caused
151 by surface heterogeneity. Due to the lack of available observational data for many cities in 2013 and
152 2014, we did not develop models for these two years. In our approach, 80% of the dataset is used for
153 model training, while the remaining 20% is reserved for testing. We perform ten-fold cross-validation
154 and assess model performance using seven statistical metrics, as listed in Table S2.

155 Following the construction of the machine learning models for individual cities and years, we
156 introduce the FEA approach. The key principle of FEA is the assumption that the total emissions of ozone
157 precursors remain unchanged from the baseline year. Specifically, we establish hourly-resolution models
158 for the baseline year (i) during the summer season (June to August) as a reference for anthropogenic
159 emissions, represented by the pink solid line in Fig. 1. These models are then applied to predict ozone
160 concentrations under the meteorological conditions of the prediction year (j), while holding the emission
161 levels constant at those of the baseline year (i), as shown by the blue solid line in Fig. 1. The difference
162 between the predicted values ($Pred_i$) and the observed values (OBS_i) for the baseline year (i) represents
163 the model residuals (RES_i), as shown in Eq. (1). The difference in observed MDA8 ozone concentrations
164 between baseline year i and prediction year j is driven by the differences in meteorological conditions
165 $MET_{i(j)}$ and anthropogenic emission controls $ANT_{i(j)}$ (Eq. 2). The prediction result $Pred_{i(j)}$ obtained
166 by applying the model trained with data from year i to the meteorological conditions of year j , the
167 difference between $Pred_{i(j)}$ and Baseline ($Pred_i$) is driven by $MET_{i(j)}$, while the difference between
168 $Pred_{i(j)}$ and the observed levels in year j (OBS_j), minus the RES_i , yields the ozone variation driven by

169 ($ANT_{i(j)}$). Therefore, $MET_{i(j)}$ and $ANT_{i(j)}$ can be quantified and calculated using Eqs. (3-4).

170
$$OBS_i = Pred_i + RES_i, \quad (1)$$

171
$$OBS_{i(j)} = MET_{i(j)} + ANT_{i(j)}, \quad (2)$$

172
$$MET_{i(j)} = Pred_{i(j)} - Pred_i, \quad (3)$$

173
$$ANT_{i(j)} = OBS_j - Pred_{i(j)} - RES_i, \quad (4)$$

174 The difference in observed MDA8 ozone concentrations between two different prediction years (j_1 ,
175 j_2) is driven by the differences in meteorological conditions ($\Delta MET_{i(j_1,j_2)}$) and anthropogenic emission
176 controls ($\Delta ANT_{i(j_1,j_2)}$) (Eq. 5). The term $\Delta MET_{i(j_1,j_2)}$ represents the changes in meteorological
177 conditions and can be calculated by the difference between the predicted values, $Pred_{i(j_1)}$ and
178 $Pred_{i(j_2)}$, for the corresponding years (Eq. 6). Similarly, the value of $\Delta ANT_{i(j_1,j_2)}$, representing the
179 change in anthropogenic emissions between the two years j_1 and j_2 , can be therefore calculated using Eq.
180 (7). By performing these calculations, we can isolate and quantify the contributions of meteorological
181 conditions and anthropogenic emission controls to the observed ozone trends. We used a cross-matrix
182 research method to assess the uncertainty of FEA, with specific formulas available in Supporting Method
183 S2.

184
$$\Delta OBS_{(j_1,j_2)} = \Delta MET_{i(j_1,j_2)} + \Delta ANT_{i(j_1,j_2)}, \quad (5)$$

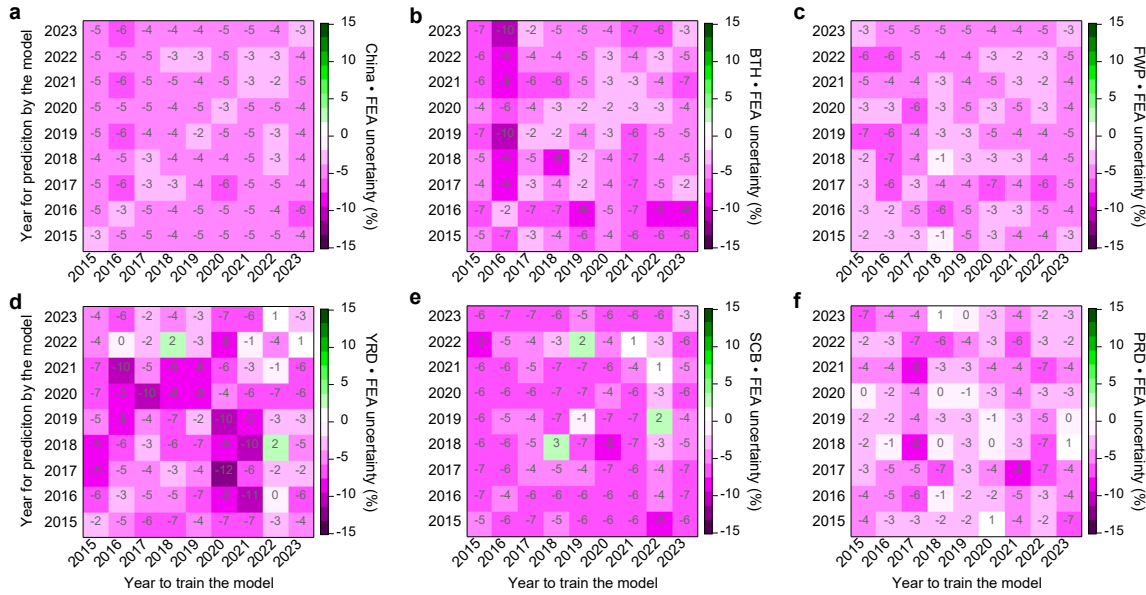
185
$$\Delta MET_{i(j_1,j_2)} = Pred_{i(j_2)} - Pred_{i(j_1)}, \quad (6)$$

186
$$\Delta ANT_{i(j_1,j_2)} = ANT_{i(j_2)} - ANT_{i(j_1)} = (OBS_{j_2} - Pred_{i(j_2)} - RES_i) - (OBS_{j_1} - Pred_{i(j_1)} - RES_i)$$

187
$$= (OBS_{j_2} - OBS_{j_1}) - (Pred_{i(j_2)} - Pred_{i(j_1)}), \quad (7)$$

188 Model performance was first evaluated through ten-fold cross-validation for the BTH region,
189 revealing high predictive skill between observed and predicted MDA8 ozone levels during 2015-2023
190 (Fig. S2). The index of agreement (IOA) ranged from 0.96 to 0.97, with correlation coefficients (R)
191 between 0.93 and 0.95. Root mean square errors (RMSE) and normalized mean bias (NMB) varied from
192 16.9 to 21.9 $\mu\text{g m}^{-3}$ and 8 to 25%, respectively, indicating high model accuracy. Nationally, the model
193 yielded R values of 0.88–0.91 and IOA of 0.93–0.95, with errors remaining within acceptable ranges
194 (Tables S3–S8). To assess uncertainty stemming from interannual model training variability, we applied
195 a matrix-based resampling approach (see Text S2). As shown in Fig. 2, the relative difference in residuals

196 ranged from -9% to 3%, and remained within $\pm 12\%$ for all regions – supporting the robustness of the
 197 FEA method. Notably, inclusion of time-related variables could reduce model uncertainty compared to
 198 simulations excluding these predictors. The average uncertainty decreased by approximately 2–4% at the
 199 regional-mean level (Fig. S3).



200 **Figure 2. Uncertainty assessment of the FEA method.** The uncertainty for the FEA method is calculated using the
 201 approach described in Text S2. The x-axis represents the years used for model training, and the y-axis represents the
 202 years predicted by the trained model. The diagonal line in each sub-panel represents the changes in the residuals of
 203 the models.

205 2.3 Weather normalization analysis

206 To compare the FEA method with other commonly used statistical approaches, we also applied the
 207 widely adopted meteorological normalization technique based on the RF algorithm (Grange et al., 2018;
 208 Vu et al., 2019). This approach constructs a regression model that relates air pollutant concentrations to
 209 meteorological parameters and emission surrogate indicators (i.e., time variables such as unix time, day
 210 of year, day of month, and hour of day) (Grange et al., 2018; Vu et al., 2019). Once the model is trained,
 211 air pollutant concentrations are predicted by randomly resampling meteorological variables from long-
 212 term historical meteorological datasets, thereby generating a new ensemble of predictions (Vu et al.,
 213 2019). These predictions are made under consistent meteorological conditions, enabling the isolation of
 214 meteorological influences from anthropogenic emission effects on air pollutant trends. The resulting
 215 weather-normalized pollutant concentrations (Fig. 1) represent the levels expected under average
 216 meteorological conditions, thus reflecting the impact of emission changes alone. In this study, the

217 meteorological normalization follows this established framework, with meteorological variables
218 randomly sampled from the long-term dataset spanning 1970-2023. Each normalization process involves
219 1,000 iterations, and the arithmetic mean of these iterations' simulated values was adopted as the final
220 normalized result. The alignment between FEA-based and weather-normalized trends (Fig. S4) affirms
221 the robustness of the FEA framework.

222 **2.3 Quantification of extreme weather-driven changes in ozone**

223 An unprecedented and persistent heatwave struck central and eastern China during the summer of
224 2022, with the Yangtze River Delta (YRD) experiencing the most severe impacts (Wang et al., 2023b;
225 Zhang et al., 2023). This event has been identified as the longest-lasting and most intense heatwave since
226 at least 1961 (Mallapaty, 2022). In contrast, the Yangtze-Huaihe region is climatologically prone to
227 sustained extreme precipitation, where prolonged rainfall episodes frequently occur during the East Asian
228 summer monsoon (Yin et al., 2020). Together, the extreme heatwave (HW) in 2022 and recurrent
229 prolonged rainfall (PR) events provide unique and physically realistic atmospheric conditions to
230 investigate the impacts of typical weather extremes on surface ozone.

231 To quantify the contributions of extreme meteorological conditions to ozone variability, we applied
232 the SHapley Additive exPlanations (SHAP) method (Lundberg et al., 2020) to interpret predictions from
233 the random forest model. SHAP assigns an importance value to each input feature k , representing its
234 marginal contribution to the model-predicted MDA8 ozone. The PR period was defined as 15 June to 15
235 July for each year, while the remaining period from June to August was classified as the non-prolonged
236 rainfall (NPR) period. The HW event in 2022 was defined as 16 July to 31 August, with the same calendar
237 period in other years designated as non-heatwave (NHW) conditions.

238 SHAP values were calculated for all input features during the PR and NPR periods, as well as during
239 the HW and NHW periods, respectively. The relative changes in SHAP values ($\Delta SHAP$) between these
240 conditions were used to assess the responses of MDA8 ozone to the rainy season or the 2022 heatwave
241 weather conditions, as per the following Eqs:

$$242 \Delta SHAP_k = SHAP_{PR} - SHAP_{NPR} \quad (8)$$

$$243 \Delta SHAP_k = SHAP_{HW} - SHAP_{NHW} \quad (9)$$

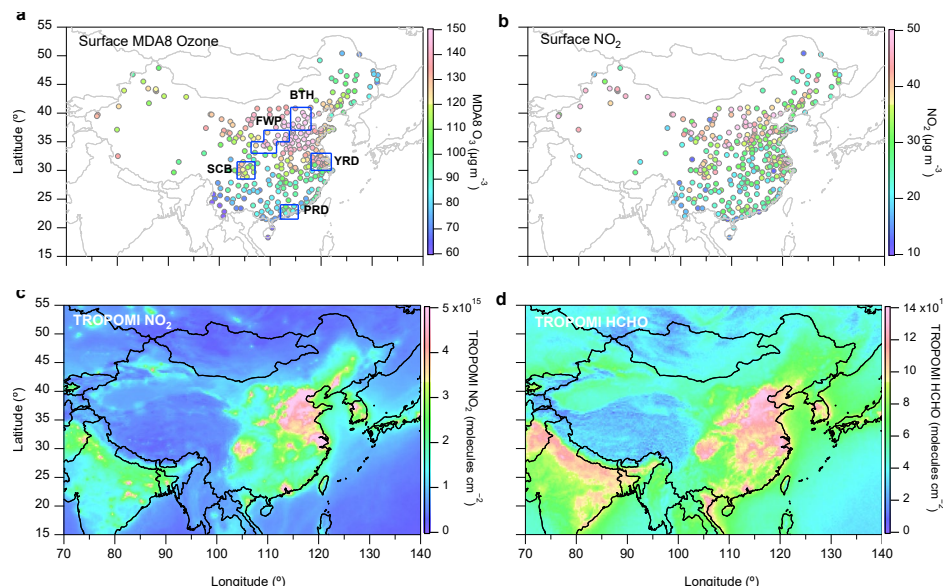
244 **2.5 FEA-based assessment of climate change impacts on ozone**

245 To evaluate the long-term impact of climate change on surface ozone concentrations across
246 China from 1970 to 2023, we extended the framework of our machine learning-based FEA method.
247 The core idea of this analysis is to isolate the influence of long-term meteorological variability on
248 ozone while assuming fixed anthropogenic emissions. Given the availability of relatively complete
249 and continuous hourly ozone observations and meteorological data from 2015 to 2023, this period
250 was used to construct nine emission baseline scenarios. Following the modeling protocol described in
251 Section 2.2, nine independent random forest models were trained for each city and scenario, with each
252 year from 2015 to 2023 serving as an emissions reference. Model inputs included hourly ozone
253 observations, key meteorological predictors, and time-related variables (hour of day and month of year).
254 The trained models were then applied to historical meteorological reanalysis data from 1970 to 2023 to
255 simulate ozone trends under fixed emissions (Fig. 1), yielding nine independent ozone trajectories, each
256 reflecting the influence of long-term meteorological variability under a different fixed-emissions
257 assumption. While the choice of emission baseline may affect the absolute magnitude of simulated ozone,
258 it does not alter the primary objective: assessing the sensitivity of surface ozone to meteorological drivers
259 over multidecadal timescales (Lecœur et al., 2014; Leung et al., 2018; Wang et al., 2022b). This approach
260 could capture the climate-induced ozone signal while adopting the common assumption that emissions
261 are not themselves influenced by climate change – a simplification consistent with prior attribution
262 studies (Dang and Liao, 2019; Leung et al., 2018; Shen et al., 2017; Wang et al., 2022b). For comparison,
263 we also estimated the impact of anthropogenic emission changes on ozone concentrations during 2015–
264 2023 using the same FEA methodology and the complete hourly dataset for model training. This dual-
265 track analysis enables a clear distinction between the impacts of climate variability and emission
266 mitigation on observed ozone trends.

267 To examine the sensitivity of urban ozone pollution to climate variability under different potential
268 atmospheric conditions (e.g., oxidation capacity) and its possible evolution under global warming, we
269 defined three representative regional scenarios based on typical ozone pollution characteristics in China
270 (Fig. 3a): a high-pollution scenario for BTH (BaseBTH), a moderate-pollution scenario for YRD
271 (BaseYRD), and a low-pollution scenario for Pearl River Delta (PRD) (BasePRD). These scenarios allow
272 assessment of ozone trends and climate impacts under fixed emissions across three distinct atmospheric
273 conditions.

274 **3 Results and Discussion**275 **3.1 Spatiotemporal variation of summertime ozone**

276 Figure 3 presents the spatial distribution of the average summertime (2018-2023) maximum daily
 277 8-hour average (MDA8) ozone, surface NO_2 , and TROPOMI NO_2 , HCHO column concentrations across
 278 China, along with the locations of the country's five typical city clusters: **BTH**, **Fenwei Plain (FWP)**,
 279 **YRD**, **Sichuan Basin (SCB)**, and **PRD**. Across these five city clusters, the average summer ozone
 280 concentrations ranged from 88.9 to $161.3 \mu\text{g m}^{-3}$ – substantially exceeding the $43.0 \mu\text{g m}^{-3}$ threshold
 281 associated with ecosystem productivity loss (Gong et al., 2021) and the World Health Organization
 282 (WHO, 2021) recommended peak seasonal average of $60 \mu\text{g m}^{-3}$. TROPOMI satellite observations of
 283 NO_2 column concentration show notably elevated concentrations over the five city clusters, particularly
 284 in the BTH, YRD, and FWP, which align with surface NO_2 distribution patterns and confirm the scale of
 285 anthropogenic NO_x emissions in these regions (Zheng et al., 2021). TROPOMI satellite observations of
 286 HCHO column concentrations similarly reveal these city clusters as hotspots for VOC emissions (Fig.
 287 3d). These concurrent high levels of NO_2 and HCHO suggest a strong photochemical ozone pollution
 288 potential, as the abundant precursors in these urban clusters could drive substantial ozone production
 289 during the summer months.



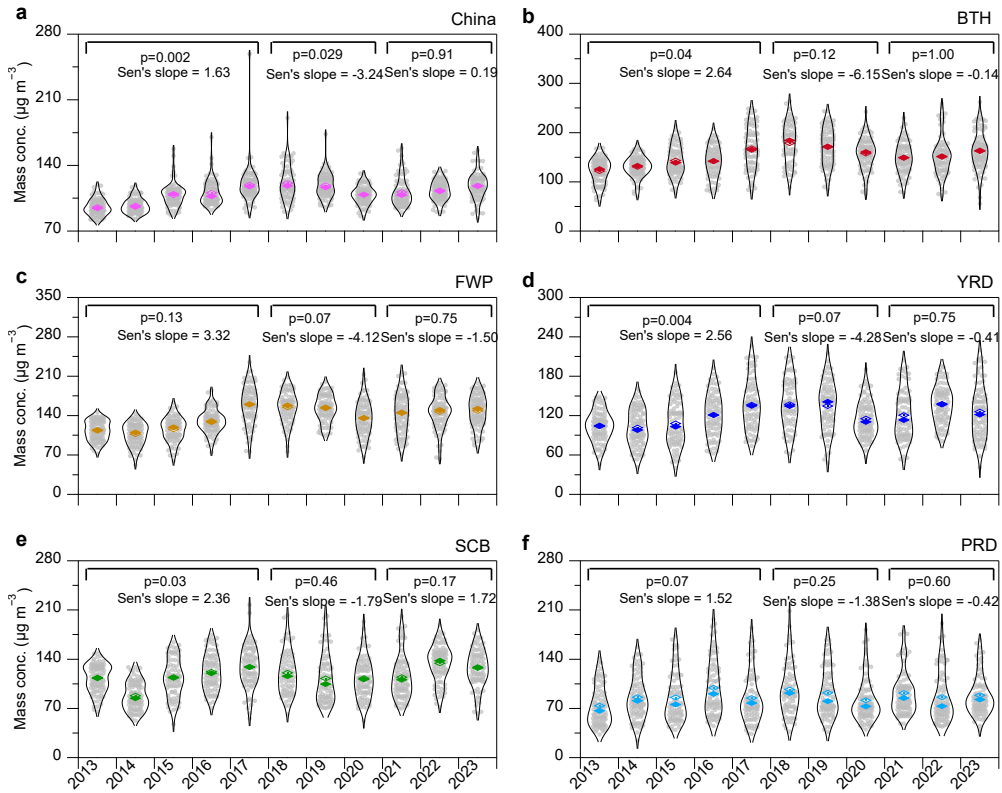
290
 291 **Figure 3. Spatial distribution of summertime MDA8 ozone, surface NO_2 , and TROPOMI NO_2 , HCHO across**
 292 **major city clusters in China.** The panels represent the average MDA8 ozone, surface NO_2 , and TROPOMI NO_2 ,
 293 HCHO column concentrations for 354 cities in China during the summertime (June–August) from 2018 to 2023.
 294 The corresponding five regions includes BTH (37° – 41°N , 114° – 118°E); YRD (30° – 33°N , 118.2° – 122°E); SCB

295 (28.5°–31.5°N, 103.5°–107°E); PRD (21.5°–24°N, 112°–115.5°E) and FWP (106.25°–111.25°E, 33°–35°N, and
296 108.75°–113.75°E, 35°–37°N).

297

298 Figure 4 presents the interannual variations in MDA8 ozone concentrations during summertime
299 across China, with a focus on the five city cluster regions. During the **Phase I** (2013–2017), the average
300 nationwide MDA8 ozone increased significantly ($p < 0.01$), rising from 95.5 to 118.0 $\mu\text{g m}^{-3}$. This growth
301 was especially pronounced in the BTH and FWP regions, where the concentrations increased by
302 approximately 38% and 41%, respectively. In contrast, ozone increases were more modest in the YRD
303 (~11%), SCB (~15%), and PRD (~16%) regions, respectively. These results were consistent with the
304 previous studies (Li et al., 2021; Liu and Wang, 2020a, 2020b; Wang et al., 2023a). Corresponding to the
305 implementation of more stringent emission controls on NO_x and VOCs emissions during the **Phase II**
306 (Geng et al., 2024; Liu et al., 2023), a moderate national decrease in MDA8 ozone was observed, with
307 concentrations declining to 109.0 $\mu\text{g m}^{-3}$ from 2017 to 2020. The declines during this period were most
308 notable in FWP (~16%) and YRD (~15%), while BTH (~6%), SCB (~11%), and PRD (~4%) also showed
309 reductions compared to their concentration peaks observed in 2017. However, the MDA8 ozone
310 rebounded, reaching 118.4 $\mu\text{g m}^{-3}$ in 2023 – comparable to its 2017 peak – with a particularly sharp
311 increase during the summer of 2022. From 2021 to 2023, MDA8 ozone concentrations rose by 2.8 $\mu\text{g m}^{-3}$
312 in BTH, 3.1 $\mu\text{g m}^{-3}$ in FWP, 16.1 $\mu\text{g m}^{-3}$ in YRD, and 18.5 $\mu\text{g m}^{-3}$ in SCB, respectively.

313 Figure S1 further illustrates the spatiotemporal evolution of summertime MDA8 ozone in China
314 from 2013 to 2023. On average, approximately 68% of the cities exceeded the WHO air quality guideline
315 of 100 $\mu\text{g m}^{-3}$ for the MDA8 ozone. Elevated ozone levels were primarily observed in densely populated
316 and economically developed regions. Spatially, ozone hotspot regions expanded between 2013 and 2017
317 (Fig. S1 a–e), followed by contraction during 2018–2020 (Fig. S1 f–i). However, this progress stalled in
318 2021. A sharp reversal was observed in 2022, with widespread increases in MDA8 ozone (Fig. S1 k).
319 These changes could be closely linked to emission control measures and meteorological conditions,
320 which will be further discussed in Sections 3.2 and 3.3.



321

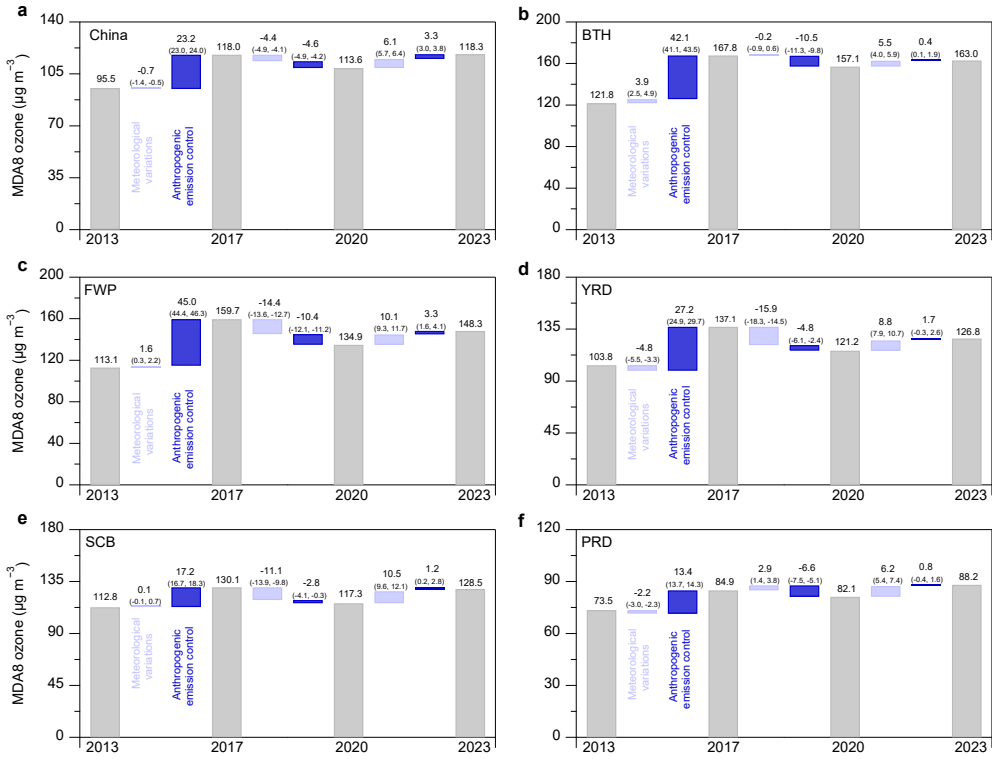
322 **Figure 4. Interannual trends of summertime MDA8 ozone across China (2013–2023).** **a** the seasonal variations
 323 of MDA8 ozone during the summer months (June, July, and August) over China. **b-f** the average trend across the
 324 five city cluster regions in China: BTH, FWP, YRD, SCB, and PRD, respectively. The summer months are defined
 325 according to meteorological seasonality, encompassing June, July, and August. In the violin plots, hollow diamond
 326 markers denote the mean, while solid diamond markers represent the median. The Mann-Kendall test and Sen's slope
 327 estimator were employed to assess the statistical significance and rate of change in the monthly average MDA8
 328 ozone concentrations. The *p* value represents the significance level from the Mann-Kendall test, which is used to
 329 determine the statistical significance of the trend in the data.

330

331 3.2 Anthropogenic emission drivers of ozone trends

332 To disentangle the relative impacts of anthropogenic emissions and meteorological variability on
 333 observed ozone trends, we applied the machine learning-based FEA framework described in Section 2.2.
 334 As illustrated in Fig. 5, anthropogenic emissions were the dominant driver of ozone increases during
 335 2013–2017, contributing an average rise of approximately $23.2 \pm 1.1 \mu\text{g m}^{-3}$ nationwide. The most
 336 pronounced increases occurred in the FWP and BTH ($45.0 \pm 2.0 \mu\text{g m}^{-3}$ and $42.1 \pm 2.0 \mu\text{g m}^{-3}$,
 337 respectively), whereas the PRD exhibited a relatively modest enhancement ($13.4 \pm 1.6 \mu\text{g m}^{-3}$), reflecting
 338 its predominantly NO_x -limited photochemical regime versus VOC-limited regimes in other regions (Ren
 339 et al., 2022). As shown in Fig. S5, the precursor gases NO_2 and CO exhibited regionally distinct

340 decreasing trends, partially explaining the spatial heterogeneity of ozone changes. The MDA8 ozone
341 decreased by $10.5 \pm 2.0 \mu\text{g m}^{-3}$ in BTH and $10.4 \pm 3.0 \mu\text{g m}^{-3}$ in FWP, with smaller declines in YRD ($-4.8 \pm 3.8 \mu\text{g m}^{-3}$), SCB ($-2.8 \pm 2.4 \mu\text{g m}^{-3}$), and PRD ($-6.6 \pm 1.4 \mu\text{g m}^{-3}$) between 2017 and 2020 (Fig. 5).
342 These trends were overall consistent with those derived using independent statistical approaches (Wang
343 et al., 2023). The COVID-19 pandemic (January-April 2020) introduced an unprecedented perturbation
344 to anthropogenic activity, leading to sharp declines in industrial production, energy consumption, and
345 transportation (Shi and Brasseur, 2020; Zheng et al., 2021). National emissions of SO_2 , NO_x , $\text{PM}_{2.5}$, and
346 VOCs were estimated to have decreased by 0.37 Tg (12%), 0.87 Tg (13%), 0.25 Tg (10%), and 1.07 Tg
347 (12%), respectively, relative to the same period in 2019 (Geng et al., 2024). Despite these reductions,
348 MDA8 ozone concentrations increased by $1.7\text{--}2.3 \mu\text{g m}^{-3}$ across BTH, FWP, YRD, and SCB, while a
349 slight decrease occurred in PRD (Fig. S6). Overall, $\sim 79\%$ of monitored cities experienced ozone
350 increases, with a national mean enhancement of $2.1 \pm 1.3 \mu\text{g m}^{-3}$ (Fig. S7). In the post-pandemic period
351 (2020-2023), concentrations of NO_2 , CO, and $\text{PM}_{2.5}$ stabilized or declined more gradually (Fig. S5), and
352 the contribution of anthropogenic emissions to ozone variability weakened considerably (Fig. S8).
353 Regionally, emission-driven changes ranged from -1.2 to $+2.6 \mu\text{g m}^{-3}$ in BTH, -1.6 to $+4.0 \mu\text{g m}^{-3}$ in
354 FWP, -4.7 to $+7.4 \mu\text{g m}^{-3}$ in YRD, -3.6 to $+3.0 \mu\text{g m}^{-3}$ in SCB, and -3.8 to $+7.7 \mu\text{g m}^{-3}$ in PRD. These
355 results indicate that while emission controls initially yielded substantial ozone mitigation benefits during
356 the Phase II, their effectiveness has gradually diminished, underscoring the need for more targeted and
357 region-specific emission control strategies under evolving photochemical regimes.
358



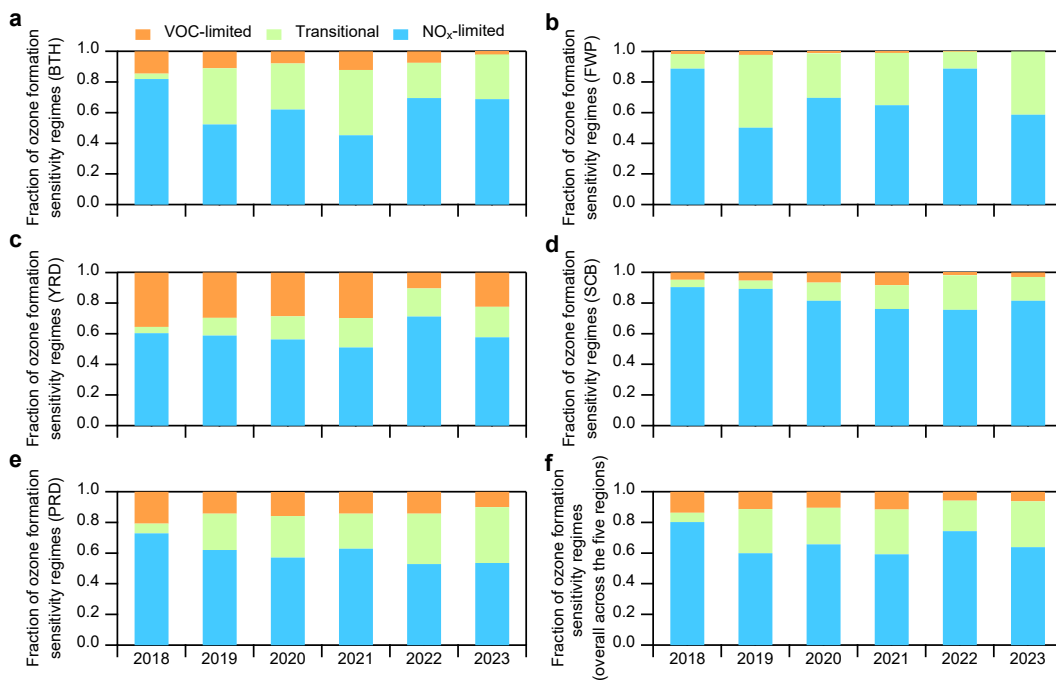
359

360 **Figure 5. Anthropogenic and meteorological drivers of ozone trends from 2013 to 2023.** Changes in summertime
 361 MDA8 ozone concentrations were decomposed into contributions from anthropogenic emissions and meteorological
 362 variability using the FEA framework. Results reflect ensemble estimates based on multiple baseline years (2015–
 363 2023) for emissions. The interquartile range, with values in parentheses denoting the 25th and 75th percentiles across
 364 all baseline scenarios.

365

366 Satellite retrievals of tropospheric NO₂ and HCHO from TROPOMI (Figs. S9–S10) further reveal
 367 evolving ozone production chemistry. NO₂ columns exhibited strong east–west gradients, with eastern
 368 China maintaining levels five times higher than the west. Between 2018 and 2023, NO₂ columns over
 369 the North China Plain (NCP) declined from 4.13×10^{15} to 3.85×10^{15} molecules cm^{-2} , while HCHO
 370 remained stable until 2021, followed by a sharp increase in 2022. The spatial pattern of temperature
 371 anomalies between heatwave and non-heatwave periods (Fig. S11) reveals strong positive differences in
 372 the YRD and SCB, consistent with enhanced biogenic and anthropogenic VOC emissions under extreme
 373 heat (Qin et al., 2025; Tao et al., 2024). By 2023, HCHO concentrations had returned to pre-heatwave
 374 levels. To diagnose the evolving chemical sensitivity of ozone production, we examined the
 375 spatiotemporal evolution of the HCHO/NO₂ ratio (Text S1). Figure S12 shows that this ratio exhibited
 376 regionally distinct transitions from 2018 to 2023, reflecting shifts in photochemical regimes. Figure 6
 377 summarizes the relative contributions of VOC-limited, NO_x-limited, and transitional regimes across the
 378 five key regions. In BTH, NO_x-limited areas accounted for ~82% of the domain in 2018 and remained

379 above 45% thereafter, while VOC-limited regions declined from ~14% to ~2%. In FWP, summer ozone
 380 formation was largely controlled by NO_x-limited and transitional regimes. The YRD underwent a notable
 381 shift from VOC- to NO_x-limited chemistry, with VOC-limited fractions decreasing from ~35% in 2018
 382 to ~22% in 2023, particularly during 2022 when extreme heat amplified VOC emissions and
 383 photochemical activity (Qin et al., 2025; Tao et al., 2024). The SCB region consistently exhibited strong
 384 NO_x limitation (>75%), whereas the PRD showed a gradual expansion of the transitional regime
 385 alongside a modest contraction of VOC-limited regions. These shifts in photochemical sensitivity
 386 correspond well with the ozone decrease observed during the Phase II emission reductions. Spatial
 387 distributions of ozone formation sensitivity during the COVID-19 lockdown (Fig. S13) reveal that most
 388 of China was in a transitional regime, with major urban clusters remaining VOC-limited and only limited
 389 areas in southern China being NO_x-limited. This spatial pattern aligns with the observed widespread
 390 ozone increases during the lockdown (Fig. S7). These findings highlight that ozone production chemistry
 391 in China was shaped by the complex interplay between emission reduction efforts and the rising
 392 frequency of meteorological extremes under a warming climate.



393 **Figure 6. Trends in the distributions of ozone production sensitivity regimes.** Fractions of VOC-limited, NO_x-
 394 limited, and transitional ozone sensitivity regimes across five key regions during the summertime (June to August)
 395 from 2018 to 2023, based on the FNR analysis. **a-e** the trend across the five city cluster regions in China during the
 396 summer months (June, July, and August): BTH, FWP, YRD, SCB, and PRD, respectively. **f** presents the overall
 397 trends for all five regions.

399 **3.3 Meteorological impact on ozone variation**

400 Figure 5 shows the interannual meteorological contributions to summertime MDA8 ozone across
401 different emission-control phases. During the Phase I, meteorology exerted relatively weak influences
402 on ozone variability, with contributions ranging from -4.8 to $+3.9 \mu\text{g m}^{-3}$ —far smaller than those from
403 anthropogenic emission changes. In contrast, meteorological anomalies became a decisive factor from
404 2017 to 2020, driving substantial ozone reductions. Ozone decreases attributable to meteorology reached
405 $-14.4 \pm 3.0 \mu\text{g m}^{-3}$ in the FWP, $-15.9 \pm 3.8 \mu\text{g m}^{-3}$ in the YRD, and $-11.1 \pm 2.4 \mu\text{g m}^{-3}$ in the SCB,
406 explaining $58 \pm 12\%$, $77 \pm 18\%$, and $80 \pm 17\%$ of the total ozone decline, respectively. A notable shift
407 occurred from 2020 to 2023, when the influence of extreme meteorological events increasingly
408 dominated ozone variability. In the summer of 2022, persistent heatwaves across eastern and southern
409 China (Mallapaty, 2022; Wang et al., 2023b) triggered sharp ozone increases of $+20.8 \pm 3.6 \mu\text{g m}^{-3}$ in
410 the YRD and $+22.1 \pm 3.2 \mu\text{g m}^{-3}$ in the SCB, reflecting the enhanced photochemical activity under high-
411 temperature and intense solar radiation conditions. The following summer (2023) featured anomalously
412 heavy rainfall, resulting in sharp ozone suppression ($-17.8 \pm 2.3 \mu\text{g m}^{-3}$ in the YRD and $-9.7 \pm 3.3 \mu\text{g}$
413 m^{-3} in the SCB). This reduction coincided with a remarkable increase in precipitation, i.e., 102% in YRD
414 and 35% in SCB (Fig. S14), **indicating that rainy meteorological conditions may have suppressed ozone**
415 **production.**

416 To identify the dominant meteorological drivers, we analyzed Gini importance scores derived from
417 the RF model across 18 predictor variables (Fig. S15). Temperature (T) emerged as the most influential
418 predictor in the BTH and FWP regions, while shortwave solar radiation (SR), relative humidity (RH),
419 and 850hPa zonal wind (u850) were most important in the YRD. In the PRD, ozone variability was
420 primarily governed by temperature and transport-related indices, including meridional winds at different
421 altitudes. These findings are consistent with the climatological contrast between northern continental and
422 southern coastal regimes: in northern China, stagnant anticyclonic conditions (Gong and Liao, 2019) and
423 strong solar radiation promote photochemical production (Bao et al., 2025), whereas in southern regions,
424 high humidity and convective rainfall could tend to suppress ozone by reducing actinic flux and
425 enhancing removal of precursors(Lu et al., 2019).

426 Partial dependence analysis (Fig. S16) further illustrates the nonlinear responses of ozone to key
427 meteorological factors (T, RH, and SR) for representative cities in each cluster, revealing clear regional

428 contrasts. In Beijing (BTH), ozone concentrations show the strongest positive response to T (Fig. S16a),
429 consistent with the enhancement of reaction kinetics and biogenic VOC emissions under hot conditions.
430 This behavior reflects the thermodynamic coupling between surface heating, boundary-layer expansion,
431 and photochemical production. In Nanjing (YRD), ozone was more sensitive to solar radiation than to
432 temperature (Fig. S16c), highlighting the dominant role of actinic flux in controlling radical production
433 during warm and dry conditions. **Consistent with these findings, Yang et al. (2024) reported that high-**
434 **temperature and low-RH conditions over the NCP and YRD could enhance photochemical ozone**
435 **formation, with chemical production dominating during peak pollution periods.** In the SCB, both T and
436 RH exhibited strong influences, while ozone variability was shaped primarily by T and large-scale
437 circulation patterns in the PRD associated with subtropical maritime flow and typhoon incursions from
438 the Northwest Pacific (Chen et al., 2024; Wang et al., 2024a; Wang et al., 2022a).

439 To further quantify these relationships, we applied SHAP (SHapley Additive exPlanations) analysis
440 to evaluate the meteorological influence of the HW and the PR events in the Yangtze-Huaihe region
441 between 2015 and 2023 (Section 2.4). As shown in Fig. S17, the HW events were associated with strong
442 positive SHAP values in southeastern coastal areas, especially the YRD and SCB, driven by elevated SR
443 and T . Mean SR during the HW periods was substantially higher than during the non-HW periods (Fig.
444 S18), increasing photochemical activity through increased radical generation and faster reaction rates.
445 Conversely, PR events produced consistent negative SHAP contributions across all regions (Fig. S19),
446 reflecting the combined effects of reduced photolysis, increased humidity, and efficient wet scavenging
447 on ozone production (He and Carmichael, 1999). A multi-year comparison (Fig. 7) highlights the
448 opposing effects of key meteorological variables – including RH, T , boundary layer height (BLH), total
449 precipitation (TP), and surface pressure (SP) – on MDA8 ozone. The trend in Δ SHAP values under
450 high-humidity conditions from 2015 to 2023 (Fig. S20) further confirms the model’s ability to capture
451 the suppressive effects of wet weather conditions on ozone formation.

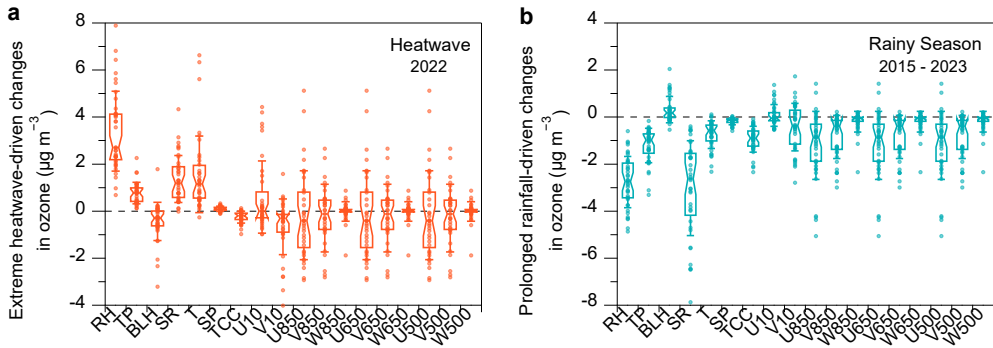


Figure 7. Meteorological impact on predicted ozone concentrations under heatwave and rainy weather conditions. (a) Differences in SHAP values (ΔSHAP) between heatwave and non-heatwave periods in the Yangtze-Huaihe region during summer 2022. (b) Differences in SHAP values (ΔSHAP) between prolonged rainfall periods and non-prolonged rainfall periods in the same region from 2015 to 2023. Box plots show the distribution of ΔSHAP across cities; the center line indicates the median, boxes denote the interquartile range (25th-75th percentiles), and the whisker line extends to one standard deviation.

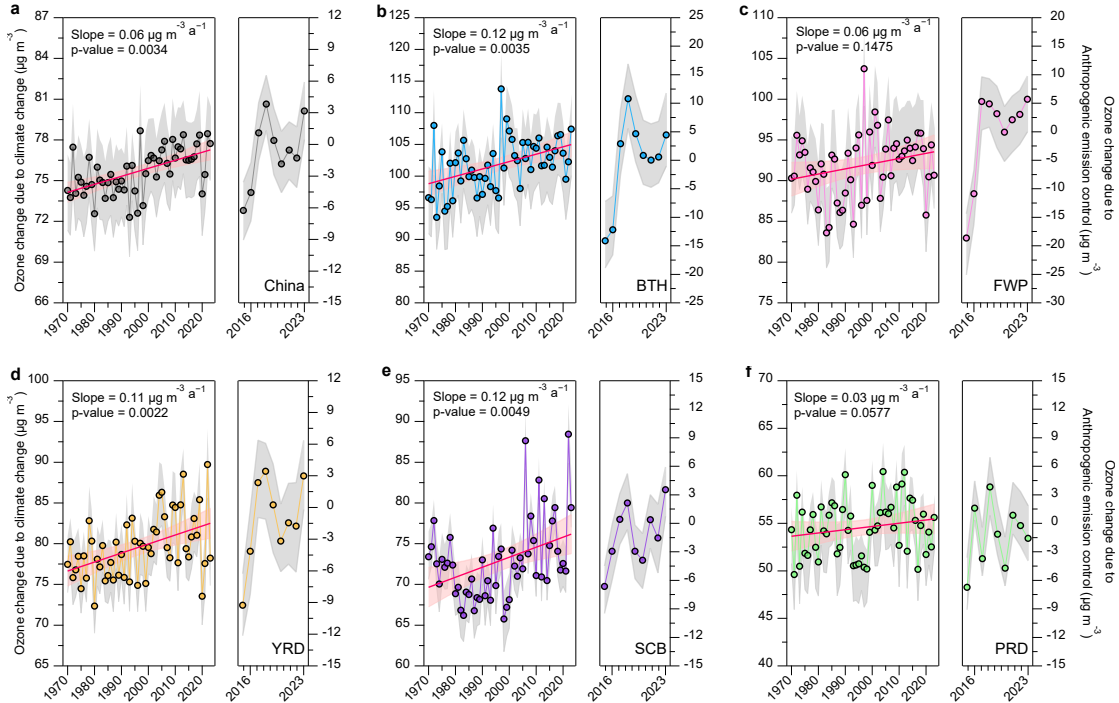
3.4 Reshaping distributions of ozone by climate change and emission controls

To assess the long-term influence of climate change on surface ozone concentrations, we applied the FEA framework to simulate summertime ozone trends over the period 1970 – 2023. In this analysis, anthropogenic emissions were held constant at their 2015 – 2023 summertime levels, while interannual variations in meteorological variables were introduced using historical reanalysis data. This design isolates the climate-driven component of ozone trends while assuming that emission trajectories are independent of climate change – a simplification aligned with prior attribution frameworks (Wang et al., 2022b). The impact of anthropogenic emission controls was estimated by comparing observed ozone concentrations with FEA-predicted values during 2015 – 2023, thereby quantifying the residual effect of emissions under fixed meteorology.

As shown in Fig. 8, under the 2015-2023 emission levels, climate change has exerted a statistically significant ($p < 0.05$) positive influence on urban summertime ozone concentrations across China, resulting in a nationwide increase of approximately $0.06 \mu\text{g m}^{-3} \text{ yr}^{-1}$ since 1970. All five major urban regions displayed upward trends, with the most pronounced increase observed in the BTH and SCB at $0.12 \mu\text{g m}^{-3} \text{ yr}^{-1}$. Three sensitivity simulations (see Section 2.5 and Fig. S21) confirm this robustness: trend slopes range from 0.11 – $0.14 \mu\text{g m}^{-3} \text{ yr}^{-1}$ in BaseBTH (high-pollution scenario), 0.05 – $0.10 \mu\text{g m}^{-3} \text{ yr}^{-1}$ in the BaseYRD (moderate-pollution scenario), and 0.03 – $0.10 \mu\text{g m}^{-3} \text{ yr}^{-1}$ in the BasePRD (low-pollution scenario). Despite regional differences in chemical regimes or pollution levels, the consistent

478 upward tendencies underscore the pervasive climatic amplification of ozone formation. These results
479 emphasize that climate change acts as a systematic driver of ozone growth across diverse atmospheric
480 environments, reinforcing the need to embed climate resilience within emission control strategies. Spatial
481 correlations between climate-driven ozone increases and temperature changes (Fig. S22) further confirm
482 that warming is the dominant contributor to long-term ozone enhancement. In particular, the correlation
483 coefficients between ozone trends and temperature anomalies reached 0.90 (BTH), 0.89 (FWP), 0.72
484 (YRD), and 0.93 (SCB), indicating a strong temperature dependence of climate-induced ozone formation
485 in these regions. The PRD showed a weaker correlation, likely due to its unique subtropical maritime
486 climate and higher humidity and cloud cover, which tend to suppress photochemical ozone production
487 (Yang et al., 2019). The right panel of Fig. 8 depicts summertime ozone trends from 2015 to 2023 under
488 the combined influence of anthropogenic emissions, derived from the FEA method. Ozone
489 concentrations rose across all regions between 2015 and 2018, declined modestly during 2018-2020, and
490 rebounded thereafter in most regions except the PRD.

491 These findings are consistent with future projections that anticipate more frequent high-ozone
492 episodes under continued warming (Li et al., 2023). Recent analyses (Yang et al., 2024) show that the
493 frequency of high-temperature and low-humidity conditions during 2000-2019 was markedly higher than
494 in 1980-1999, suggesting that ozone pollution in both the NCP and YRD has intensified under historical
495 climate change. Indeed, while national emission controls curbed ozone growth after 2018, a post-2020
496 rebound has emerged, implying that the climatic penalty on ozone is beginning to offset emission gains.
497 The extreme 2022 heatwave exemplified this effect, substantially enhancing photochemical activity and
498 shifting ozone sensitivity from VOC-limited to transitional or NO_x-limited regimes. Although reductions
499 in anthropogenic precursor emissions have improved ozone control efficiency, the warming-induced
500 enhancement of ozone increasingly interferes with – and in some regions may partially offset – the air-
501 quality gains achieved through emission reduction efforts.



502

503 **Figure 8. Impact of climate change and emission controls on ozone trends.** Left panels show ozone trends
 504 attributable to long-term climate change from 1970 to 2023, simulated under fixed emission scenarios using the FEA
 505 framework. Right panels depict ozone trends from 2015 to 2023, reflecting the impact of anthropogenic emission
 506 controls. Each trajectory represents results based on a distinct emissions baseline year. Shaded grey areas indicate
 507 the interquartile range (25th-75th percentiles), solid red lines denote trend estimates, and light red shading marks the
 508 5th-95th percentile confidence intervals. Statistical significance and trend slopes were assessed using the Mann-
 509 Kendall test. More details of the sensitivity tests are provided in Fig. S18.

510

4 Conclusions and implications

511 In this study, we developed a machine learning-based FEA framework to disentangle and quantify the
 512 respective roles of anthropogenic emissions and meteorological drivers in shaping ozone trends during
 513 2013-2023. With a national-level prediction uncertainty of approximately 6%, the FEA method provides
 514 a computationally efficient and scalable tool for diagnosing atmospheric variability across large spatial
 515 and temporal domains. However, the current model framework did not explicitly resolve grid-scale
 516 spatial heterogeneity, vegetation feedbacks, or land-use dynamics, which may influence the ozone
 517 prediction. In addition, the sensitivity of the results to spatial resolution need further investigation
 518 through coupled applications of machine learning and chemical transport models.

519

Our results revealed that increased anthropogenic emissions were the dominant driver of the sharp
 rise in summertime MDA8 ozone concentrations during the Phase I, contributing an average increase of

521 $23.2 \pm 1.1 \text{ } \mu\text{g m}^{-3}$. In contrast, the strengthened clean air actions during the Phase II – particularly the
522 synergistic control of NO_x and VOCs – led to measurable reductions in MDA8 ozone, with national-
523 average declines of $4.6 \pm 1.5 \text{ } \mu\text{g m}^{-3}$ from 2017 to 2020. These improvements were especially evident in
524 regions such as BTH and FWP, where ozone formation was highly sensitive to VOCs. However, the
525 impact of emission reductions diminished considerably during the recent period (2021–2023). This
526 stagnation underscores the urgent need for more targeted, region-specific emission control strategies that
527 address the shifting photochemical sensitivity of ozone formation regimes.

528 Using the SHAP attribution analysis, we further quantified the influence of meteorological extremes
529 on ozone variability. Record-breaking heatwaves in 2022 enhanced ozone concentrations by up to $+5.8$
530 $\mu\text{g m}^{-3}$, while prolonged pluvial episodes, particularly during the East Asian monsoon season, suppressed
531 ozone by as much as $-15.2 \mu\text{g m}^{-3}$. These results highlight the dominance of short-term meteorological
532 extremes in shaping ozone air quality under a warming climate. Complementary satellite-based FNR
533 diagnostics revealed that most urban clusters remain VOC-limited or transitional, except the PRD, which
534 is largely NO_x -limited. The 2022 heatwave induced regime shifts in regions such as the YRD, where
535 intensified VOC emissions and elevated temperatures drove transitions toward NO_x -limited conditions.
536 These findings emphasize the need for dynamic, region-specific assessments of ozone sensitivity to guide
537 effective mitigation strategies.

538 To assess the climate penalty on ozone, we extended the FEA framework to simulate long-term
539 trends from 1970 to 2023 by fixing emissions and allowing meteorological variables to evolve with
540 observed climate trends. Our findings show that climate change has contributed to a significant upward
541 trend in urban summertime ozone, averaging $0.06 \mu\text{g m}^{-3} \text{ a}^{-1}$, with particularly strong increases in the
542 BTH and SCB. Good correlations between the modelled ozone and surface temperature ($r = 0.72\text{--}0.93$)
543 across major urban clusters indicated that climate warming exerts a persistent control on the long-term
544 evolution of ozone. While reductions in precursor emissions have improved ozone control efficiency, the
545 direct enhancement of ozone by rising temperatures increasingly interferes with, and in some regions
546 may partially offset, the air-quality benefits achieved through emission mitigation. Together, these
547 findings highlight that effective ozone management in a warming world will require integrated strategies
548 that jointly address emission reductions and climate adaptation.

549

550 *Data availability.* Data are provided within the manuscript or supplementary information files.

551

552 *Code availability.* The statistical computing in this study was based on R language software which can
553 be download at <https://www.r-project.org/>.

554

555 *Author contributions.*

556 Y.Z. and X.G. initiated and designed the study. Y.Z. and JF developed the statistical methodology, model
557 calculation, and data analysis. J.F. and Y.Z. prepared the manuscript with contributions from D.H., B.Z.,
558 M.W., J.L., Y.S., H.L., J.W., Y.W., B.Y., M.C., and X.G..

559

560 *Competing interests.* The authors declare no competing interests.

561

562 *Acknowledgments.*

563 This study was supported by the National Key Research and Development Program of China (grant
564 2023YFC3706200), the National Natural Science Foundation of China (grant no. 42207124) and Natural
565 Science Foundation of Jiangsu Province (grant no. BK20210663).

566

567 **Correspondence** and requests for materials should be addressed to Yunjiang Zhang.

568

569 **References**

570 Agathokleous, E., Feng, Z., Oksanen, E., Sicard, P., Wang, Q., Saitanis, C.J., Araminiene, V., Blande,
571 J.D., Hayes, F., Calatayud, V., Domingos, M., Veresoglou, S.D., Peñuelas, J., Wardle, D.A., De Marco,
572 A., Li, Z., Harmens, H., Yuan, X., Vitale, M., Paoletti, E.: Ozone affects plant, insect, and soil microbial
573 communities: A threat to terrestrial ecosystems and biodiversity, *Sci. Adv.*, 6, eabc1176,
574 <https://doi.org/10.1126/sciadv.abc1176>, 2020.

575 Bao, J., Li, X., Kong, L., Li, J., Chen, Q., Zhang, Y.: Comparative analysis of the impact of rising
576 temperatures on ozone levels in China and the United States, *npj Clean Air*, 1, 23,
577 <https://doi.org/10.1038/s44407-025-00023-8>, 2025.

578 Chen, S., Wang, H., Lu, K., Zeng, L., Hu, M., Zhang, Y.: The trend of surface ozone in Beijing from 2013
579 to 2019: Indications of the persisting strong atmospheric oxidation capacity, *Atmos. Environ.*, 242,
580 117801, <https://doi.org/10.1016/j.atmosenv.2020.117801>, 2020.

581 Chen, Y., Lu, X., Fung, J.C.H.: Spatiotemporal source apportionment of ozone pollution over the Greater
582 Bay Area, *Atmos. Chem. Phys.*, 24, 8847-8864, <https://doi.org/10.5194/acp-24-8847-2024>, 2024.

583 Dai, Q., Dai, T., Hou, L., Li, L., Bi, X., Zhang, Y., Feng, Y.: Quantifying the impacts of emissions and
584 meteorology on the interannual variations of air pollutants in major Chinese cities from 2015 to 2021,
585 *Sci. China Earth Sci.*, 66, 1725-1737, <https://doi.org/10.1007/s11430-022-1128-1>, 2023.

586 Dang, R., Liao, H.: Severe winter haze days in the Beijing–Tianjin–Hebei region from 1985 to 2017 and
587 the roles of anthropogenic emissions and meteorology, *Atmos. Chem. Phys.*, 19, 10801-10816,
588 <https://doi.org/10.5194/acp-19-10801-2019>, 2019.

589 Fishman, J., Ramanathan, V., Crutzen, P.J., Liu, S.C.: Tropospheric ozone and climate, *Nature*, 282, 818-
590 820, <https://doi.org/10.1038/282818a0>, 1979.

591 Gao, M., Wang, F., Ding, Y., Wu, Z., Xu, Y., Lu, X., Wang, Z., Carmichael, G.R., McElroy, M.B.: Large-
592 scale climate patterns offer preseasonal hints on the co-occurrence of heat wave and O₃ pollution in
593 China, *Proc. Natl. Acad. Sci. USA*, 120, e2218274120, <https://doi.org/10.1073/pnas.2218274120>,
594 2023.

595 Geng, G., Liu, Y., Liu, Y., Liu, S., Cheng, J., Yan, L., Wu, N., Hu, H., Tong, D., Zheng, B., Yin, Z., He,
596 K., Zhang, Q.: Efficacy of China's clean air actions to tackle PM_{2.5} pollution between 2013 and 2020,
597 *Nat. Geosci.*, 17, 987-994, <https://doi.org/10.1038/s41561-024-01540-z>, 2024.

598 Geng, G., Xiao, Q., Liu, S., Liu, X., Cheng, J., Zheng, Y., Xue, T., Tong, D., Zheng, B., Peng, Y., Huang,
599 X., He, K., Zhang, Q.: Tracking Air Pollution in China: Near real-time PM_{2.5} retrievals from
600 multisource data fusion, *Environ. Sci. Technol.*, 55, 12106-12115,
601 <https://doi.org/10.1021/acs.est.1c01863>, 2021.

602 Gong, C., Liao, H.: A typical weather pattern for ozone pollution events in North China, *Atmos. Chem.
603 Phys.*, 19, 13725-13740, <https://doi.org/10.5194/acp-19-13725-2019>, 2019.

604 Gong, C., Yue, X., Liao, H., Ma, Y.M.: A humidity-based exposure index representing ozone damage
605 effects on vegetation, *Environ. Res. Lett.*, 16, <https://doi.org/10.1088/1748-9326/abecbb>, 2021.

606 Grange, S.K., Carslaw, D.C., Lewis, A.C., Boleti, E., Hueglin, C.: Random forest meteorological
607 normalisation models for Swiss PM₁₀ trend analysis, *Atmos. Chem. Phys.*, 18, 6223-6239,
608 <https://doi.org/10.5194/acp-18-6223-2018>, 2018.

609 Guo, J., Zhang, X., Gao, Y., Wang, Z., Zhang, M., Xue, W., Herrmann, H., Brasseur, G.P., Wang, T.,
610 Wang, Z.: Evolution of ozone pollution in China: what track will it follow? *Environ. Sci. Technol.*, 57,
611 109-117, <https://doi.org/10.1021/acs.est.2c08205>, 2023.

612 Hallquist, M., Munthe, J., Hu, M., Wang, T., Chan, C.K., Gao, J., Boman, J., Guo, S., Hallquist, Å.M.,
613 Mellqvist, J., Moldanova, J., Pathak, R.K., Pettersson, J.B.C., Pleijel, H., Simpson, D., Thynell, M.:
614 Photochemical smog in China: scientific challenges and implications for air-quality policies, *Natl. Sci.*
615 *Rev.*, 3, 401-403, <https://doi.org/10.1093/nsr/nww080>, 2016.

616 Hauglustaine, D.A., Granier, C., Brasseur, G.P., Mégie, G.: The importance of atmospheric chemistry in
617 the calculation of radiative forcing on the climate system, *J. Geophys. Res.*, 99, 1173-1186,
618 <https://doi.org/10.1029/93JD02987>, 1994.

619 He, S., Carmichael, G.R.: Sensitivity of photolysis rates and ozone production in the troposphere to
620 aerosol properties, *J. Geophys. Res. Atmos.*, 104, 26307-26324.
621 <https://doi.org/10.1029/1999JD900789>, 1999.

622 IPCC, 2021. Annex I: Observational Products [Trewin, B. (ed.)], in: Masson-Delmotte, V., Zhai, P., Pirani,
623 A., Connors, S.L., Péan, C., Berger, S., Caud, N., Chen, Y., Goldfarb, L., Gomis, M.I., Huang, M.,
624 Leitzell, K., Lonnoy, E., Matthews, J.B.R., Maycock, T.K., Waterfield, T., Yelekçi, O., Yu, R., Zhou,
625 B. (Eds.), *Climate Change 2021: The Physical Science Basis. Contribution of Working Group I to the*
626 *Sixth Assessment Report of the Intergovernmental Panel on Climate Change*. Cambridge University
627 Press, Cambridge, United Kingdom and New York, NY, USA, pp. 2061–2086.

628 Ivatt, P.D., Evans, M.J., Lewis, A.C.: Suppression of surface ozone by an aerosol-inhibited
629 photochemical ozone regime, *Nat. Geosci.*, 15, 536-540, <https://doi.org/10.1038/s41561-022-00972-9>, 2022.

630 Jacob, D.J.: Heterogeneous chemistry and tropospheric ozone, *Atmos. Environ.*, 34, 2131-2159,
631 [https://doi.org/10.1016/S1352-2310\(99\)00462-8](https://doi.org/10.1016/S1352-2310(99)00462-8), 2000.

632 Knowlton, K., Rosenthal, J.E., Hogrefe, C., Lynn, B., Gaffin, S., Goldberg, R., Rosenzweig, C., Civerolo,
633 K., Ku, J.-Y., Kinney, P.L.: Assessing Ozone-related health impacts under a changing climate, *Environ.*
634 *Health Perspect.*, 112, 1557-1563, <https://doi.org/10.1289/ehp.716>, 2004.

635 Lamsal, L.N., Krotkov, N.A., Celarier, E.A., Swartz, W.H., Pickering, K.E., Bucsela, E.J., Gleason, J.F.,
636 Martin, R.V., Philip, S., Irie, H., Cede, A., Herman, J., Weinheimer, A., Szykman, J.J., Knepp, T.N.:
637 Evaluation of OMI operational standard NO₂ column retrievals using in situ and surface-based NO₂
638 observations, *Atmos. Chem. Phys.*, 14, 11587-11609, <https://doi.org/10.5194/acp-14-11587-2014>,
639 2014.

640 Lecœur, È., Seigneur, C., Pagé, C., Terray, L.: A statistical method to estimate PM_{2.5} concentrations from
641 meteorology and its application to the effect of climate change, *J. Geophys. Res. Atmos.*, 119, 3537-
642 3585, <https://doi.org/10.1002/2013JD021172>, 2014.

643 Leung, D.M., Tai, A.P.K., Mickley, L.J., Moch, J.M., van Donkelaar, A., Shen, L., Martin, R.V.: Synoptic
644 meteorological modes of variability for fine particulate matter (PM_{2.5}) air quality in major metropolitan
645 regions of China, *Atmos. Chem. Phys.*, 18, 6733-6748, <https://doi.org/10.5194/acp-18-6733-2018>,
646 2018.

647 Li, H., Yang, Y., Jin, J., Wang, H., Li, K., Wang, P., Liao, H.: Climate-driven deterioration of future ozone
648 pollution in Asia predicted by machine learning with multi-source data, *Atmos. Chem. Phys.*, 23, 1131-
649 1145, <https://doi.org/10.5194/acp-23-1131-2023>, 2023.

650 Li, J., Wang, S., Zhu, J., Wang, D., Zhao, T.: Accelerated shifts from heatwaves to heavy rainfall in a
651 changing climate, *npj Clim. Atmos. Sci.* 8, 214, <https://doi.org/10.1038/s41612-025-01113-w>, 2025a.

652 Li, K., Jacob, D.J., Liao, H., Shen, L., Zhang, Q., Bates, K.H.: Anthropogenic drivers of 2013–2017
653 trends in summer surface ozone in China, *Proc. Natl. Acad. Sci. USA*, 116, 422-427,
654 <https://doi.org/10.1073/pnas.1812168116>, 2019a.

655

656 Li, K., Jacob, D.J., Liao, H., Zhu, J., Shah, V., Shen, L., Bates, K.H., Zhang, Q., Zhai, S.: A two-pollutant
657 strategy for improving ozone and particulate air quality in China, *Nat. Geosci.*, 12, 906-910,
658 <https://doi.org/10.1038/s41561-019-0464-x>, 2019b.

659 Li, K., Jacob, D.J., Shen, L., Lu, X., De Smedt, I., Liao, H.: Increases in surface ozone pollution in China
660 from 2013 to 2019: anthropogenic and meteorological influences, *Atmos. Chem. Phys.*, 20, 11423-
661 11433, <https://doi.org/10.5194/acp-20-11423-2020>, 2020.

662 Li, M., Wang, T., Shu, L., Qu, Y., Xie, M., Liu, J., Wu, H., Kalsoom, U.: Rising surface ozone in China
663 from 2013 to 2017: A response to the recent atmospheric warming or pollutant controls? *Atmos.*
664 *Environ.*, 246, 118130, <https://doi.org/10.1016/j.atmosenv.2020.118130>, 2021.

665 Li, S., Wu, L., Wang, Y., Geng, T., Cai, W., Gan, B., Jing, Z., Yang, Y. Intensified Atlantic multidecadal
666 variability in a warming climate, *Nat. Clim. Change*, 15, 293-300, <https://doi.org/10.1038/s41558-025-02252-x>, 2025b.

667 Liu, C., Shi, K.: A review on methodology in O₃-NO_x-VOC sensitivity study, *Environ. Pollut.*, 291,
668 118249, <https://doi.org/10.1016/j.envpol.2021.118249>, 2021.

669 Liu, Y., Geng, G., Cheng, J., Liu, Y., Xiao, Q., Liu, L., Shi, Q., Tong, D., He, K., Zhang, Q.: Drivers of
670 increasing ozone during the two phases of clean air actions in China 2013–2020, *Environ. Sci. Technol.*,
671 57, 8954-8964, <https://doi.org/10.1021/acs.est.3c00054>, 2023.

672 Liu, Y., Wang, T. Worsening urban ozone pollution in China from 2013 to 2017 – Part 1: The complex
673 and varying roles of meteorology, *Atmos. Chem. Phys.*, 20, 6305-6321, <https://doi.org/10.5194/acp-20-6305-2020>, 2020a.

674 Liu, Y., Wang, T.: Worsening urban ozone pollution in China from 2013 to 2017 – Part 2: The effects of
675 emission changes and implications for multi-pollutant control, *Atmos. Chem. Phys.*, 20, 6323-6337,
676 <https://doi.org/10.5194/acp-20-6323-2020>, 2020b.

677 Lu, X., Zhang, L. & Shen, L.: Meteorology and climate influences on tropospheric ozone: a review of
678 natural sources, chemistry, and transport patterns. *Curr. Pollution Rep.* 5, 238 – 260,
679 <https://doi.org/10.1007/s40726-019-00118-3>, 2019.

680 Lundberg, S.M., Erion, G., Chen, H., DeGrave, A., Prutkin, J.M., Nair, B., Katz, R., Himmelfarb, J.,
681 Bansal, N., Lee, S.I.: From local explanations to global understanding with explainable AI for trees.
682 *Nat. Mach. Intell.*, 2, 56-67, <https://doi.org/10.1038/s42256-019-0138-9>, 2020.

683 Ma, X., Yin, Z.: Dipole pattern of summer ozone pollution in the east of China and its connection with
684 climate variability, *Atmos. Chem. Phys.*, 21, 16349-16361, <https://doi.org/10.5194/acp-21-16349-2021>, 2021.

685 Mallapaty, S.: China's extreme weather challenges scientists trying to study it, *Nature*, 609, 888-888,
686 <https://doi.org/10.1038/d41586-022-02954-8>, 2022.

687 Meng, Q., Zhang, Y., Zhong, S., Fang, J., Tang, L., Rao, Y., Zhou, M., Qiu, J., Xu, X., Petit, J.-E.J.A.C.,
688 Physics: Reconstructing missing surface aerosol elemental carbon data in long-term series with
689 ensemble learning, *Atmos. Chem. Phys.*, 25, 7485-7498, <https://doi.org/10.5194/acp-25-7485-2025>,
690 2025.

691 Pu, X., Wang, T.J., Huang, X., Melas, D., Zanis, P., Papanastasiou, D.K., Poupkou, A.: Enhanced surface
692 ozone during the heat wave of 2013 in Yangtze River Delta region, China, *Sci. Total Environ.*, 603-
693 604, 807-816, <https://doi.org/10.1016/j.scitotenv.2017.03.056>, 2017.

694 Qin, M., She, Y., Wang, M., Wang, H., Chang, Y., Tan, Z., An, J., Huang, J., Yuan, Z., Lu, J., Wang, Q.,
695 Liu, C., Liu, Z., Xie, X., Li, J., Liao, H., Pye, H.O.T., Huang, C., Guo, S., Hu, M., Zhang, Y., Jacob,
696 D.J., Hu, J.: Increased urban ozone in heatwaves due to temperature-induced emissions of

700 anthropogenic volatile organic compounds, *Nat. Geosci.*, 18, 50-56, <https://doi.org/10.1038/s41561-024-01608-w>, 2025.

701

702 Ren, J., Guo, F., Xie, S.: Diagnosing ozone-NO_x-VOC sensitivity and revealing causes of ozone
703 increases in China based on 2013–2021 satellite retrievals, *Atmos. Chem. Phys.*, 22, 15035-15047,
704 <https://doi.org/10.5194/acp-22-15035-2022>, 2022.

705 Shen, L., Jacob, D.J., Zhu, L., Zhang, Q., Zheng, B., Sulprizio, M.P., Li, K., De Smedt, I., González Abad,
706 G., Cao, H., Fu, T.-M., Liao, H.: The 2005–2016 trends of formaldehyde columns over China observed
707 by satellites: increasing anthropogenic emissions of volatile organic compounds and decreasing
708 agricultural fire emissions, *Geophys. Res. Lett.*, 46, 4468-4475, <https://doi.org/10.1029/2019GL082172>, 2019.

709

710 Shen, L., Mickley, L.J., Murray, L.T.: Influence of 2000–2050 climate change on particulate matter in
711 the United States: results from a new statistical model, *Atmos. Chem. Phys.*, 17, 4355-4367,
712 <https://doi.org/10.5194/acp-17-4355-2017>, 2017.

713 Shi, X., Brasseur, G.P.: The response in air quality to the reduction of Chinese economic activities during
714 the COVID-19 outbreak, *Geophys. Res. Lett.*, 47, e2020GL088070,
715 <https://doi.org/10.1029/2020GL088070>, 2020.

716 Shi, Z., Song, C., Liu, B., Lu, G., Xu, J., Van Vu, T., Elliott, R.J.R., Li, W., Bloss, W.J., Harrison, R.M.:
717 Abrupt but smaller than expected changes in surface air quality attributable to COVID-19 lockdowns,
718 *Sci. Adv.*, 7, eabd6696, <https://doi.org/10.1126/sciadv.abd6696>, 2021.

719 Tao, C., Zhang, Y., Zhang, X., Guan, X., Peng, Y., Wang, G., Zhang, Q., Ren, Y., Zhao, X., Zhao, R.,
720 Wang, Q., Wang, W.: Discrepant global surface ozone responses to emission- and heatwave-induced
721 regime shifts, *Environ. Sci. Technol.*, 58, 22288-22297, <https://doi.org/10.1021/acs.est.4c08422>, 2024.

722 Vu, T.V., Shi, Z., Cheng, J., Zhang, Q., He, K., Wang, S., Harrison, R.M.: Assessing the impact of clean
723 air action on air quality trends in Beijing using a machine learning technique, *Atmos. Chem. Phys.*, 19,
724 11303-11314, <https://doi.org/10.5194/acp-19-11303-2019>, 2019.

725 Wang, J., Wang, P., Tian, C., Gao, M., Cheng, T., Mei, W.: Consecutive Northward super typhoons
726 induced extreme ozone pollution events in Eastern China, *npj Clim. Atmos.*, *Sci.*, 7, 244,
727 <https://doi.org/10.1038/s41612-024-00786-z>, 2024a.

728 Wang, L., Chen, B., Ouyang, J., Mu, Y., Zhen, L., Yang, L., Xu, W., Tang, L.: Causal-inference machine
729 learning reveals the drivers of China's 2022 ozone rebound, *Environ. Sci. Ecotech.*, 24, 100524,
730 <https://doi.org/10.1016/j.ese.2025.100524>, 2025.

731 Wang, M., Chen, X., Jiang, Z., He, T.-L., Jones, D., Liu, J., Shen, Y.: Meteorological and anthropogenic
732 drivers of surface ozone change in the North China Plain in 2015–2021, *Sci. Total Environ.*, 906,
733 167763, <https://doi.org/10.1016/j.scitotenv.2023.167763>, 2024b.

734 Wang, N., Huang, X., Xu, J., Wang, T., Tan, Z.-m., Ding, A.: Typhoon-boosted biogenic emission
735 aggravates cross-regional ozone pollution in China, *Sci. Adv.*, 8, eabl6166,
736 <https://doi.org/10.1126/sciadv.abl6166>, 2022b.

737 Wang, R., Yang, Y., Xing, X., Wang, L., Chen, J., Tang, X., Cao, J., Morawska, L., Balkanski, Y.,
738 Hauglustaine, D., Ciais, P., Ma, J.: Stringent emission controls are needed to reach clean air targets for
739 cities in China under a warming climate, *Environ. Sci. Technol.*, 56, 11199-11211,
740 <https://doi.org/10.1021/acs.est.1c08403>, 2022c.

741 Wang, T., Xue, L., Brimblecombe, P., Lam, Y.F., Li, L., Zhang, L.: Ozone pollution in China: A review
742 of concentrations, meteorological influences, chemical precursors, and effects, *Sci. Total Environ.*,
743 575, 1582-1596, <https://doi.org/10.1016/j.scitotenv.2016.10.081>, 2017.

744 Wang, Y., Zhao, Y., Liu, Y., Jiang, Y., Zheng, B., Xing, J., Liu, Y., Wang, S., Nielsen, C.P.: Sustained
745 emission reductions have restrained the ozone pollution over China, *Nat. Geosci.*, 16, 967-974,
746 <https://doi.org/10.1038/s41561-023-01284-2>, 2023a.

747 Wang, Z.Q., Luo, H.L., Yang, S.: Different mechanisms for the extremely hot central-eastern China in
748 July-August 2022 from a Eurasian large-scale circulation perspective, *Environ. Res. Lett.*,
749 18,<https://doi.org/10.1088/1748-9326/acb3e5>, 2023b.

750 Weng, X., Forster, G.L., Nowack, P.: A machine learning approach to quantify meteorological drivers of
751 ozone pollution in China from 2015 to 2019, *Atmos. Chem. Phys.*, 22, 8385-8402,
752 <https://doi.org/10.5194/acp-22-8385-2022>, 2022.

753 World Health Organization (2021), WHO global air quality guidelines. Particulate matter (PM2.5 and
754 PM10), ozone, nitrogen dioxide, sulfur dioxide and carbon monoxide. ISBN 978-92-4-003422-8Wu,
755 K., Wang, Y., Qiao, Y., Liu, Y., Wang, S., Yang, X., Wang, H., Lu, Y., Zhang, X., Lei, Y.: Drivers of
756 2013–2020 ozone trends in the Sichuan Basin, China: Impacts of meteorology and precursor emission
757 changes, *Environ. Pollut.*, 300, 118914, <https://doi.org/10.1016/j.envpol.2022.118914>, 2022.

758 Xue, L., Ding, A., Cooper, O., Huang, X., Wang, W., Zhou, D., Wu, Z., McClure-Begley, A.,
759 Petropavlovskikh, I., Andreae, M.O., Fu, C.: ENSO and Southeast Asian biomass burning modulate
760 subtropical trans-Pacific ozone transport, *Natl. Sci. Rev.*, 8, <https://doi.org/10.1093/nsr/nwaa132>, 2020.

761 Yang, L., Luo, H., Yuan, Z., Zheng, J., Huang, Z., Li, C., Lin, X., Louie, P.K.K., Chen, D., Bian, Y.:
762 Quantitative impacts of meteorology and precursor emission changes on the long-term trend of
763 ambient ozone over the Pearl River Delta, China, and implications for ozone control strategy, *Atmos.*
764 *Chem. Phys.*, 19, 12901-12916, <https://doi.org/10.5194/acp-19-12901-2019>, 2019.

765 Yang, Y., Zhou, Y., Wang, H., Li, M., Li, H., Wang, P., Yue, X., Li, K., Zhu, J., Liao, H.: Meteorological
766 characteristics of extreme ozone pollution events in China and their future predictions, *Atmos. Chem.*
767 *Phys.*, 24, 1177-1191, <https://doi.org/10.5194/acp-24-1177-2024>, 2024.

768 Yao, T., Lu, S., Wang, Y., Li, X., Ye, H., Duan, Y., Fu, Q., Li, J. Revealing the drivers of surface ozone
769 pollution by explainable machine learning and satellite observations in Hangzhou Bay, China, *J. Clean.*
770 *Prod.*, 440, 140938, <https://doi.org/10.1016/j.jclepro.2024.140938>, 2024.

771 Ye, X., Zhang, L., Wang, X., Lu, X., Jiang, Z., Lu, N., Li, D., Xu, J.: Spatial and temporal variations of
772 surface background ozone in China analyzed with the grid-stretching capability of GEOS-Chem High
773 Performance, *Sci. Total Environ.*, 914, 169909, <https://doi.org/10.1016/j.scitotenv.2024.169909>, 2024.

774 Yin, Y., Han, C., Yang, G., Huang, Y., Liu, M., Wang, X.: Changes in the summer extreme precipitation
775 in the Jianghuai plum rain area and their relationship with the intensity anomalies of the south Asian
776 high, *Atmos. Res.*, 236, 104793, <https://doi.org/10.1016/j.atmosres.2019.104793>, 2020.

777 Zhai, S., Jacob, D.J., Wang, X., Shen, L., Li, K., Zhang, Y., Gui, K., Zhao, T., Liao, H.: Fine particulate
778 matter (PM_{2.5}) trends in China, 2013–2018: separating contributions from anthropogenic emissions
779 and meteorology, *Atmos. Chem. Phys.*, 19, 11031-11041, <https://doi.org/10.5194/acp-19-11031-2019>,
780 2019.

781 Zhang, D.Q., Chen, L.J., Yuan, Y., Zuo, J.Q., Ke, Z.J.: Why was the heat wave in the Yangtze River valley
782 abnormally intensified in late summer 2022? *Environ. Res. Lett.*, 18, <https://doi.org/10.1088/1748-9326/acba30>, 2023.

784 Zhang, Q., Zheng, Y., Tong, D., Shao, M., Wang, S., Zhang, Y., Xu, X., Wang, J., He, H., Liu, W., Ding,
785 Y., Lei, Y., Li, J., Wang, Z., Zhang, X., Wang, Y., Cheng, J., Liu, Y., Shi, Q., Yan, L., Geng, G., Hong,
786 C., Li, M., Liu, F., Zheng, B., Cao, J., Ding, A., Gao, J., Fu, Q., Huo, J., Liu, B., Liu, Z., Yang, F., He,
787 K., Hao, J.: Drivers of improved PM_{2.5} air quality in China from 2013 to 2017, *Proc. Natl. Acad. Sci.*

788 USA, 116, 24463-24469, <https://doi.org/10.1073/pnas.1907956116>, 2019.

789 Zhang, Y., Li, N., Tang, K., Wang, M., Li, H., Li, K., Zheng, B., Zhang, Q., Gao, M., Fang, J.J.S.A.:
790 Widespread surface ozone reduction triggered by dust storm disturbance on ozone production and
791 destruction chemistry. *Sci. Adv.*, 11, eadr4297, <https://doi.org/10.1126/sciadv.adr4297>, 2025.

792 Zheng, B., Tong, D., Li, M., Liu, F., Hong, C., Geng, G., Li, H., Li, X., Peng, L., Qi, J., Yan, L., Zhang,
793 Y., Zhao, H., Zheng, Y., He, K., Zhang, Q.: Trends in China's anthropogenic emissions since 2010 as
794 the consequence of clean air actions, *Atmos. Chem. Phys.*, 18, 14095-
795 14111, <https://doi.org/10.5194/acp-18-14095-2018>, 2018.

796 Zheng, B., Zhang, Q., Geng, G., Chen, C., Shi, Q., Cui, M., Lei, Y., He, K.: Changes in China's
797 anthropogenic emissions and air quality during the COVID-19 pandemic in 2020, *Earth Syst. Sci. Data*,
798 13, 2895-2907, <https://doi.org/10.5194/essd-13-2895-2021>, 2021.

799 Zheng, H., Kong, S., Zhai, S., Sun, X., Cheng, Y., Yao, L., Song, C., Zheng, Z., Shi, Z., Harrison, R.M.:
800 An intercomparison of weather normalization of PM_{2.5} concentration using traditional statistical
801 methods, machine learning, and chemistry transport models, *npj Clim. Atmos. Sci.*, 6, 214,
802 <https://doi.org/10.1038/s41612-023-00536-7>, 2023.

803